Stable finite element analysis of viscous dusty plasma

Journal:	*Engineering Computations*
Manuscript ID	EC-06-2017-0191.R1
Manuscript Type:	Research Article
Keywords:	Viscous dusty plasma, Petrov-Galerkin approach, acoustic waves, finite elements

Stable finite element analysis of viscous dusty plasma

P. Areias[♮⋆], J.N. Sikta[♮✠] and M.P. dos Santos[♮]

August 30, 2017

[♮]Department of Physics
University of Évora
Colégio Luís António Verney
Rua Romão Ramalho, 59
7002-554 Évora, Portugal

[✠]Department of Physics
Jahangirnagar University
1342 Savar, Dhaka, Bangladesh

[⋆]CERIS/Instituto Superior Técnico, University of Lisbon

Abstract

In the context of analysis of dust acoustic (solitary) waves including viscosity, we introduce a finite element formulation of the corresponding fluid dust-acoustic wave equations. With this objective, a Petrov-Galerkin weak form with upwinding is adopted. We consider a dusty unmagnetized plasma system consisting of negatively charged dust and Boltzmann electrons and ions. Nonlinearity of ion and electron number density in terms of a electrostatic potential is included. A fully-implicit time-integration is used (backward-Euler method) which requires the first derivative of the weak form. A three-field formulation is proposed, with the dust number-density, the electrostatic potential and the dust velocity being the unknown fields. Two numerical examples are introduced and results show great promise for the proposed formulation as a predictive tool in viscous dusty plasmas.

KEYWORDS: Viscous dusty plasma, Petrov-Galerkin formulation, acoustic waves, finite elements, nonlinear fluid.

1 Introduction

Irving Langmuir [1] proposed that electrons, ions and neutrals in an ionized gas can be considered as a corpuscular material he titled plasma. It is now commonly accepted that more than 99% of the known universe (in which the dust is a omnipresent ingredient) is in the plasma state, cf. [2, 3]. Plasmas containing dust particles are important in the study of the space environment, such as asteroid zones, planetary rings (viz. Saturn rings [4]), comet tails, as well as the magnetosphere of the Earth [5]. Dusty plasmas are also observed in laboratory with Q-machines, DC discharges, and RF discharges, cf. [6]. It is known that RF discharges cause dust levitation [7]. Dusty plasmas typically contain dust grains of micrometer or sub-micrometer size which are negatively charged because of field emission, ultra-violet ray irradiation, and plasma currents [8, 9]. A quantified study of the charging process was performed by Barkan *et al.* [10]. Collective effects in micro-plasmas have been studied by Verheest [11] using many-fluid models.

We assume that dust particles have constant mass and are point charges. In addition, we consider a three component plasma consisting of electrons and ions having Boltzmann density distributions with temperatures T_e and T_i, respectively, as well as negatively charged dust by electron attachment [12, 13]. Dust are comparatively heavy particles. To simplify the treatment, thermal motion of dust is not included. This case has been identified as "cold dust" by Rao, Shukla and Yu [9]. In dust-free electron–ion plasmas, ions charge generally remains constant. However, in a dusty plasma, the charge of a particle does not remain constant, cf. [12, 6].

The presence of dust grains modifies the existing plasma wave spectra and introduces dust-acoustic waves, dust ion acoustic waves, dust lattice waves etc. [14]. In dust acoustic waves, the inertia is provided by dust particle mass and the restoring force is provided by the pressures of electrons and ions. Dust acoustic waves predicted by Rao, Shukla and Yu have been experimentally observed by Barkan *et al.* [15]. As mentioned by Merlino and Goree [6], in a dust acoustic wave neighbor, dust fluid elements are coupled by the electric field associated with the wave rather than by collisions, as they would be in a neutral gas.

According to Shukla and Mamun [3], there are two types of acoustic modes in uniform, unmagnetized, collisionless dusty plasmas with a weak Coulomb coupling between the charged dust grains: dust acoustic (DA) and dust ion-acoustic (DIA) waves. In summary,

- In DA waves [9], there is a predominance of *low-frequency* dust grain dynamics with Boltzmann electron and ion distribution.
- In DIA waves [16], dust grains are stationary, electrons follow the Boltzmann distribution and ion dynamics is predominant.

In terms of dusty plasma finite element solutions, we are not aware of antecedent contributions. However, two-fluid finite element solutions of plasmas exist, one significant solution has been developed by C.R. Sovinec's group, cf. [17, 18] using classical (continuous) Galerkin methods. Inherent instabilities caused by the convective term are dealt at the time-integration level, cf. [18]. In the work of Jardin, Breslau and Ferraro [19], the Clough-Tocher $\mathscr{C}^1$ triangular element was used to solve smooth magneto-hydrodynamic problems. If the analysis involves shock waves, discontinuous Galerkin methods (cf. [20]) have been used with success with plasmas, see Levy, Shu and Yan [21]. According to Garai *et al.* [22], viscosity should be included as an important term in dusty plasmas. Although some degree of dependence with the dust number density is observed [23], we here opt for the Newtonian model for simplicity.

With the goal of obtaining a stable solution of a shock-free problem, we opt for an implicitly integrated Petrov-Galerkin formulation, which results in a very simple but effective numerical scheme. We organize this work as follows: in Section 2 the governing equations are presented (continuity, momentum and Poisson), with the respective initial and boundary conditions. In Section 3, the weak form using a Petrov-Galerkin combination of test/trial functions is presented. This is followed, in Section 4, by the discretization using Streaming Upwind Petrov-Galerkin (SUPG) [24] shape functions. In Section 5, a set of representative numerical examples is shown, confirming the robustness in terms of mesh and step-size effects in the numerical results. Vortices are also predicted, in line with the theoretical work of Hasegawa and Shukla [25]. Finally, in Section 6, conclusions are drawn.

2 Governing equations

2.1 Characteristic quantities

We consider the following independent unknown fields:

1. n_d: number density of dust
2. $\boldsymbol{u}_d$: dust velocity
3. φ: electrostatic wave potential

Equations for a dusty plasma typically make use of normalized quantities, which in turn depend on characteristic values. We introduce the Debye length for a dusty plasma, using the ion temperature, as (see the approximation $\lambda_d \cong \lambda_i$ in [3]):

$$\lambda_i = \frac{1}{Z_i e}\sqrt{\frac{\varepsilon_0 \kappa_B T_i}{n_i}} \tag{1}$$

where ε_0 is the electric permittivity of free space, κ_B is the Boltzmann constant, T_i is the ion temperature (in Kelvin), Z_i is the ion charge number, n_i is the number density of ions and e is the electron charge. In this work, ions are positively charged and dust is negatively charged. In addition, λ_i serves as a characteristic length-scale.

The dust acoustic speed (c_{da}) for cold dust is given by (cf. [14], [12]):

$$c_{da} = \sqrt{\frac{Z_d \kappa_B T_i}{m_d}} \tag{2}$$

where Z_d is the dust charge number and m_d is the mass of a single dust grain. This is a particularization of Equation (3) in [12] by specifying $\epsilon = 1/Z_d$ in their notation. Making use of equilibrium quasi-neutrality, we have (cf. [3]):

$$n_{i0} Z_i = n_{e0} + n_{d0} Z_d \tag{3}$$

where $Z_i = 1$ considered in the remainder of this work. In (3), n_{i0}, n_{e0} and n_{d0} are the ion, electron and dust number densities for $t = 0$, which is identified as equilibrium time. Another relevant constitutive ingredient is the viscosity. The bulk viscosity ξ is introduced to account for the dilatation effect in the pressure and the shear viscosity μ is used to account for the shear strain rate effect on the stress. Viscous behavior is here introduced by a constitutive law for the Cauchy stresses as a function of the velocity gradient (see Section 3.3 of [26]):

$$\boldsymbol{\sigma} = \left(\xi - \frac{2\mu}{3}\right)(\nabla \cdot \boldsymbol{u})\,\boldsymbol{I} + \mu\left[\nabla \boldsymbol{u} + (\nabla \boldsymbol{u})^T\right] \tag{4}$$

The kinematic viscosity ν is also required:

$$\nu = \frac{\mu}{n_d m_d} \tag{5}$$

From the gradient of $\boldsymbol{u}$ we obtain the vorticity for a 2D problem as (see, e.g. [27]):

$$\omega = \left|\frac{\partial u_2}{\partial x_1} - \frac{\partial u_1}{\partial x_2}\right| \tag{6}$$

2.2 Fluid theory of the dust acoustic wave: differential equations and boundary conditions

Dust is considered cold, $T_d \ll T_i$ in the following equations. The domain under consideration is denoted by Ω and the time interval under consideration is $[0, T]$. In these conditions, we have a nonlinear electrostatic fluid flow problem. The governing equations for these unknown fields are, given that $\boldsymbol{x} \in \Omega$ and $t \in [0, T]$,

Continuity equation on $\Omega \times [0, \mathrm{T}]$:

$$\dot{n}_d + \nabla \cdot (n_d \boldsymbol{u}_d) = 0 \tag{7}$$

Momentum equation on $\Omega \times [0, \mathrm{T}]$:

$$\begin{aligned} n_d m_d \dot{\boldsymbol{u}}_d + n_d m_d \nabla \boldsymbol{u}_d \cdot \boldsymbol{u}_d + m_d c_{da}^2 \nabla n_d \\ -\nabla \cdot \boldsymbol{\sigma} - e n_d Z_d \nabla \varphi = 0 \end{aligned} \tag{8}$$

Poisson-like equation on $\Omega \times [0, \mathrm{T}]$:

$$\nabla^2 \varphi + \frac{e}{\varepsilon_0} (n_i - n_e - n_d Z_d) = 0 \tag{9}$$

complemented by the initial and boundary conditions for the unknown functions $\boldsymbol{u}_d(\boldsymbol{x}, t)$, $n_d(\boldsymbol{x}, t)$, $\varphi(\boldsymbol{x}, t)$ and $\boldsymbol{t}(\boldsymbol{x}, t) = \boldsymbol{\sigma}(\boldsymbol{x}, t) \cdot \boldsymbol{v}$:

$$\boldsymbol{u}_d(\boldsymbol{x}, 0) = \boldsymbol{u}_0(\boldsymbol{x}) \tag{10}$$

$$n_d(\boldsymbol{x}, 0) = n_{d0}(\boldsymbol{x}) \tag{11}$$

$$\boldsymbol{u}_d(\boldsymbol{x}, t)|_{\boldsymbol{x} \in \Gamma_u} = \overline{\boldsymbol{u}}(t) \tag{12}$$

$$n_d(\boldsymbol{x}, t)|_{\boldsymbol{x} \in \Gamma_n} = \overline{n}(t) \tag{13}$$

$$\varphi(\boldsymbol{x}, t)|_{\boldsymbol{x} \in \Gamma_\varphi} = \overline{\varphi}(t) \tag{14}$$

$$\nabla \varphi(\boldsymbol{x}, t)|_{\boldsymbol{x} \in \Gamma_{\varphi'}} \cdot \boldsymbol{v} = \bar{t}(t) \tag{15}$$

$$\boldsymbol{\sigma}(\boldsymbol{x}, t)\,|_{\boldsymbol{x} \in \Gamma_t} \cdot \boldsymbol{v} = \bar{\boldsymbol{t}}(\boldsymbol{x}, t) \tag{16}$$

where $\Gamma = \partial\Omega$ with Γ_u, Γ_n, Γ_φ, $\Gamma_{\varphi'}$ and Γ_t are subsets of Γ with $\Gamma = \Gamma_u \cup \Gamma_t$ and $\Gamma = \Gamma_\varphi \cup \Gamma_{\varphi'}$. We have $\boldsymbol{v}$ as the outer normal to Γ. In equation (9), the electron number density n_e, and the ion number density n_i, are given by the Boltzmann distributions, corresponding to a very low frequency wave [3]:

$$n_e = n_{e0} \exp\left[\frac{e\varphi}{\kappa_B T_e}\right] \tag{17}$$

$$n_i = n_{i0} \exp\left[-\frac{e\varphi}{\kappa_B T_i}\right] \tag{18}$$

These are our constitutive equations for n_i and n_e. Characteristic lengths based on (17-18) are obtained by linearization:

$$\lambda_e = \frac{1}{e}\sqrt{\frac{\varepsilon_0 \kappa_B T_e}{n_{e0}}} \tag{19}$$

$$\lambda_i = \frac{1}{e}\sqrt{\frac{\varepsilon_0 \kappa_B T_i}{n_{i0}}} \tag{20}$$

these are the two *initial* Debye lengths for electrons and ions. The time scale is obtained from the dust angular frequency:

$$\omega_d = Z_d e \sqrt{\frac{n_{d0}}{\varepsilon_0 m_d}} \tag{21}$$

Table 1: Relevant quantities and constants (cf. 7-18).

e	Electron charge $[1.6022 \times 10^{-19}$ C$]$
κ_B	Boltzmann constant $[1.38065 \times 10^{-23}$ m^{2}kg s^{-2}K$^{-1}]$
ε_0	Vacuum permittivity $[8.85419 \times 10^{-12}$ Fm$^{-1}]$
Z_d	Dust charge number $Z_d = -Q_d/e$
n_{d0}	Dust number density at equilibrium $\left[\mathrm{m}^{-3}\right]$
n_{i0}	Ion number density at equilibrium $[\mathrm{m}^{-3}]$. Approximation: $n_{i0} \cong Z_d n_{d0}$
n_{e0}	Electron number density at equilibrium $[\mathrm{m}^{-3}]$. Approximation: $n_{e0} \cong n_{i0}$
ξ	Bulk dynamic viscosity $\left[\mathrm{Nsm}^{-2}\right]$
μ	Shear dynamic viscosity $\left[\mathrm{Nsm}^{-2}\right]$
T_e	Electron temperature [K]
T_i	Ion temperature [K]
Z_i	Ion charge number $Z_i = Q_i/e$
m_d	Mass of a dust particle [kg]
$\varphi^\star$	Representative electrostatic potential $\varphi^\star = \frac{\kappa_B T_i}{e}$ $[\mathrm{NC}^{-1}\mathrm{m}]$
$\boldsymbol{u}_0(\boldsymbol{x})$	Initial dust velocity
$n_{d0}(\boldsymbol{x})$	Initial number density of dust
$\overline{\boldsymbol{u}}(t)$	Imposed velocity at the boundary Γ_u
$\overline{n}(t)$	Imposed density at the boundary Γ_n
$\overline{\varphi}(t)$	Imposed electrostatic potential at the boundary Γ_φ
$\bar{t}(t)$	Imposed electrostatic gradient at the boundary $\Gamma_{\varphi'}$

using the period, $T^d = \frac{2\pi}{\omega_d}$. Relevant quantities are summarized in Table 1.

Unknown fields are n_d, $\boldsymbol{u}_d$ and φ. Since n_d for $t = 0$ is known to be n_{d0}, we must transform the continuity equation to read:

$$\dot{n}^\star + \nabla \cdot \left[\left(n^\star + 1\right) \boldsymbol{u}_d\right] = 0 \tag{22}$$

where $n_d = (1 + n^\star) n_{d0}$. In equation (22) it is assumed that n_{d0} is uniform. In the Poisson-like equation, we have,

$$\nabla^2 \varphi + \frac{e}{\varepsilon_0} \left[n_i - n_e - n_{d0} \left(1 + n^\star\right) Z_d\right] = 0 \tag{23}$$

In Table 1, the conversion between eV and K is performed including the Boltzmann constant, i.e. a strictly interpretation of temperature given in eV and not eV $/\kappa_B$ in the literature is taken (values for the temperatures in eV are given by [28]):

$$T\,(\mathrm{K}) = T(\mathrm{eV}) / \left(1.16045 \times 10^4 \kappa_B\right) \tag{24}$$

A graphical interpretation of the Poisson equation (9) with one species of positive and one species of negative charges is now presented (Figure 1), relating the charge balance with the electrostatic force. In

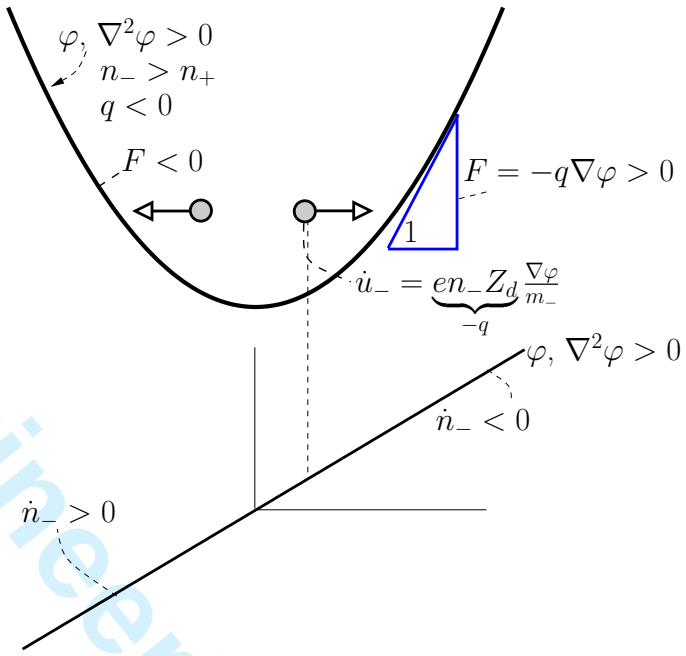

Figure 1: Graphical interpretation of the Poisson equation (9) for known φ.

the depicted case, with $\nabla^2\varphi > 0$, a outward acceleration of negatively charged particles occurs for $x \neq 0$ which in turn, due to the continuity equation (7) will decrease n_- and eventually invert the sense of $\dot{u}_-$.

3 Weak form with distinction of the convective term

Numerical time-integration of equations (7-9) is performed with the backward-Euler method. In 2D, the integrated versions of (7-9) between time-steps t_i and t_{i+1} are straightforward[1]:

$$(n^\star+1)\left(\frac{\partial u_1}{\partial x_1}+\frac{\partial u_2}{\partial x_2}\right)+\frac{n^\star_{i+1}-n^\star_i}{\Delta t}+\frac{\partial n^\star}{\partial x_1}u_1+\frac{\partial n^\star}{\partial x_2}u_2=0 \tag{25}$$

$$\begin{aligned}&(n^\star+1)\left(\frac{\boldsymbol{u}_{i+1}-\boldsymbol{u}_i}{\Delta t}\right)+(n^\star+1)\left\{\begin{array}{l} u_1\frac{\partial u_1}{\partial x_1}+u_2\frac{\partial u_1}{\partial x_2}\\ u_1\frac{\partial u_2}{\partial x_1}+u_2\frac{\partial u_2}{\partial x_2}\end{array}\right\}+\\ &-\frac{e\,(n^\star+1)\,Z_d}{m_d}\left\{\begin{array}{l}\frac{\partial\varphi}{\partial x_1}\\ \frac{\partial\varphi}{\partial x_2}\end{array}\right\}+\frac{c_{da}^2}{n_{d0}}\left\{\begin{array}{l}\frac{\partial n^\star}{\partial x_1}\\ \frac{\partial n^\star}{\partial x_2}\end{array}\right\}-\frac{1}{m_d n_{d0}}\left\{\begin{array}{l}\frac{\partial\sigma_{11}}{\partial x_1}+\frac{\partial\sigma_{21}}{\partial x_2}\\ \frac{\partial\sigma_{12}}{\partial x_1}+\frac{\partial\sigma_{22}}{\partial x_2}\end{array}\right\}=\left\{\begin{array}{l}0\\0\end{array}\right\}\end{aligned} \tag{26}$$

$$\frac{\partial^2\varphi}{\partial x_1^2}+\frac{\partial^2\varphi}{\partial x_2^2}+\frac{e}{\varepsilon_0}\left[n_i-n_e-n_{d0}\left(1+n_d^\star\right)Z_d\right]=0 \tag{27}$$

Stress components are, in 2D,

$$\sigma_{11}=2\mu\frac{\partial u_1}{\partial x_1}+\left(\xi-\frac{2\mu}{3}\right)\left(\frac{\partial u_1}{\partial x_1}+\frac{\partial u_2}{\partial x_2}\right) \tag{28}$$

$$\sigma_{22}=2\mu\frac{\partial u_2}{\partial x_2}+\left(\xi-\frac{2\mu}{3}\right)\left(\frac{\partial u_1}{\partial x_1}+\frac{\partial u_2}{\partial x_2}\right) \tag{29}$$

$$\sigma_{12}=\mu\left(\frac{\partial u_1}{\partial x_2}+\frac{\partial u_2}{\partial x_1}\right) \tag{30}$$

[1]The d subscript in $\boldsymbol{u}_d$ is omitted in this part

To make use of finite elements, equations (25-27) are now written in weak form. We introduce the following test functions:

- $\widetilde{n}^\star \in \mathscr{V}_n(\Omega)$ where $\mathscr{V}_n(\Omega) = \left\{\widetilde{n}^\star | \widetilde{n}^\star \in W^{1,2}(\Omega) \wedge \widetilde{n}(\Gamma_n) = 0\right\}$
- $\widetilde{\boldsymbol{u}} \in \mathscr{V}_u(\Omega)$ where $\mathscr{V}_u(\Omega) = \left\{\widetilde{\boldsymbol{u}} | \widetilde{\boldsymbol{u}} \in W^{1,2}(\Omega) \wedge \widetilde{u}_i(\Gamma_u) = 0\right\}$
- $\widetilde{\varphi} \in \mathscr{V}_\varphi(\Omega)$ where $\mathscr{V}_\varphi(\Omega) = \left\{\widetilde{\varphi} | \widetilde{\varphi} \in W^{1,2}(\Omega) \wedge \widetilde{\varphi}(\Gamma_\varphi) = 0\right\}$

where

$$W^{m,p}(\Omega) = \{w \in L^p(\Omega) | D^{\boldsymbol{\alpha}} w \in L^p(\Omega) \; \forall \, |\boldsymbol{\alpha}| \leq m\} \tag{31}$$

and $L^p(\Omega)$ is the space of $p-$power integrable functions. With this purpose, we use the test functions to obtain a weak form of (25-27) integrating in the domain Ω,

$$\begin{aligned}
\widetilde{W} = & \int_\Omega \widetilde{n}^\star \left[(n^\star + 1) \left(\frac{\partial u_1}{\partial x_1} + \frac{\partial u_2}{\partial x_2} \right) + \frac{n^\star_{i+1} - n^\star_i}{\Delta t} + \frac{\partial n^\star}{\partial x_1} u_1 + \frac{\partial n^\star}{\partial x_2} u_2 \right] \mathrm{d}\Omega + \\
& \int_\Omega \widetilde{\boldsymbol{u}}^T \left[(n^\star + 1) \left(\frac{\boldsymbol{u}_{i+1} - \boldsymbol{u}_i}{\Delta t} \right) - \frac{e\,(n^\star + 1)\, Z_d}{m_d} \left\{ \begin{array}{c} \frac{\partial \varphi}{\partial x_1} \\ \frac{\partial \varphi}{\partial x_2} \end{array} \right\} \right] \mathrm{d}\Omega + \\
& \int_\Omega \left[(n^\star + 1) \, \widetilde{\boldsymbol{u}}^{\bullet T} \left\{ \begin{array}{c} u_1 \frac{\partial u_1}{\partial x_1} + u_2 \frac{\partial u_1}{\partial x_2} \\ u_1 \frac{\partial u_2}{\partial x_1} + u_2 \frac{\partial u_2}{\partial x_2} \end{array} \right\} + \frac{c_{da}^2}{n_{d0}} \widetilde{\boldsymbol{u}}^T \left\{ \begin{array}{c} \frac{\partial n^\star}{\partial x_1} \\ \frac{\partial n^\star}{\partial x_2} \end{array} \right\} \right] \mathrm{d}\Omega + \\
& \int_\Omega \frac{1}{m_d n_{d0}} \left[\sigma_{11} \frac{\partial \widetilde{u}_1}{\partial x_1} + \sigma_{22} \frac{\partial \widetilde{u}_2}{\partial x_2} + \sigma_{12} \left(\frac{\partial \widetilde{u}_1}{\partial x_2} + \frac{\partial \widetilde{u}_2}{\partial x_1} \right) \right] \mathrm{d}\Omega + \\
& \int_\Omega \left\{ -\nabla \varphi \cdot \nabla \widetilde{\varphi} + \widetilde{\varphi} \frac{e}{\varepsilon_0} \left[n_i - n_e - n_{d0} \left(1 + n_d^\star \right) Z_d \right] \right\} \mathrm{d}\Omega +
\end{aligned} \tag{32}$$

$$\int_{\Gamma_{\varphi'}} \widetilde{\varphi} \underbrace{\nabla \varphi \cdot \boldsymbol{v}}_{\bar{t}} \mathrm{d}\Gamma + \int_{\Gamma_t} \widetilde{\boldsymbol{u}}^T \bar{\boldsymbol{t}} \mathrm{d}\Gamma = 0 \tag{33}$$

The non-symmetric term $\nabla \boldsymbol{u}_d \cdot \boldsymbol{u}_d$ makes use of a specific test function $\widetilde{\boldsymbol{u}}^\bullet$ to ensure a stable formulation. This will be detailed later. For the application of the Newton-Raphson method, we require the first variation of (33), for which we will make use of the symbol d:

$$\begin{aligned}
\mathrm{d}\widetilde{W} = & \int_\Omega \widetilde{n}^\star \left[\mathrm{d}n^\star \left(\frac{\partial u_1}{\partial x_1} + \frac{\partial u_2}{\partial x_2} \right) + \frac{\mathrm{d}n^\star_{i+1}}{\Delta t} \right] \mathrm{d}\Omega + \\
& \int_\Omega \widetilde{n}^\star \left[\left(\frac{\partial n^\star}{\partial x_1} \mathrm{d}u_1 + \frac{\partial n^\star}{\partial x_2} \mathrm{d}u_2 \right) + \left(\frac{\partial \mathrm{d}n^\star}{\partial x_1} u_1 + \frac{\partial \mathrm{d}n^\star}{\partial x_2} u_2 \right) \right] \mathrm{d}\Omega + \\
& \int_\Omega \widetilde{\boldsymbol{u}}^T \left[\frac{(n^\star + 1)}{\Delta t} \mathrm{d}\boldsymbol{u} + \left(\frac{\boldsymbol{u}_{i+1} - \boldsymbol{u}_i}{\Delta t} \right) \mathrm{d}n^\star \right] \mathrm{d}\Omega - \\
& \int_\Omega \widetilde{\boldsymbol{u}}^T \left[\frac{e(n^\star + 1) Z_d}{m_d} \left\{ \begin{array}{c} \frac{\partial \mathrm{d}\varphi}{\partial x_1} \\ \frac{\partial \mathrm{d}\varphi}{\partial x_2} \end{array} \right\} + \frac{\mathrm{d}n^\star e Z_d}{m_d} \left\{ \begin{array}{c} \frac{\partial \varphi}{\partial x_1} \\ \frac{\partial \varphi}{\partial x_2} \end{array} \right\} \right] \mathrm{d}\Omega + \\
& \int_\Omega (n^\star + 1) \, \widetilde{\boldsymbol{u}}^{\bullet T} \left\{ \begin{array}{c} \mathrm{d}u_1 \frac{\partial u_1}{\partial x_1} + \mathrm{d}u_2 \frac{\partial u_1}{\partial x_2} + u_1 \frac{\partial \mathrm{d}u_1}{\partial x_1} + u_2 \frac{\partial \mathrm{d}u_1}{x_2} \\ \mathrm{d}u_1 \frac{\partial u_2}{\partial x_1} + \mathrm{d}u_2 \frac{\partial u_2}{\partial x_2} + u_1 \frac{\partial \mathrm{d}u_2}{\partial x_1} + u_2 \frac{\partial \mathrm{d}u_2}{\partial x_2} \end{array} \right\} \mathrm{d}\Omega + \\
& \int_\Omega \left[(n^\star + 1) \, \mathrm{d}\widetilde{\boldsymbol{u}}^{\bullet T} \left\{ \begin{array}{c} u_1 \frac{\partial u_1}{\partial x_1} + u_2 \frac{\partial u_1}{\partial x_2} \\ u_1 \frac{\partial u_2}{\partial x_1} + u_2 \frac{\partial u_2}{\partial x_2} \end{array} \right\} + \mathrm{d}n^\star \widetilde{\boldsymbol{u}}^{\bullet T} \left\{ \begin{array}{c} u_1 \frac{\partial u_1}{\partial x_1} + u_2 \frac{\partial u_1}{\partial x_2} \\ u_1 \frac{\partial u_2}{\partial x_1} + u_2 \frac{\partial u_2}{\partial x_2} \end{array} \right\} \right] \mathrm{d}\Omega + \\
& \frac{c_{da}^2}{n_{d0}} \int_\Omega \widetilde{\boldsymbol{u}}^T \nabla \mathrm{d}n^\star \mathrm{d}\Omega + \\
& \frac{1}{m_d n_{d0}} \int_\Omega \left[\sigma_{11} \frac{\partial \mathrm{d}\widetilde{u}_1}{\partial x_1} + \sigma_{22} \frac{\partial \mathrm{d}\widetilde{u}_2}{\partial x_2} + \sigma_{12} \left(\frac{\partial \mathrm{d}\widetilde{u}_1}{\partial x_2} + \frac{\partial \mathrm{d}\widetilde{u}_2}{\partial x_1} \right) \right] \mathrm{d}\Omega + \\
& \frac{1}{m_d n_{d0}} \int_\Omega \left[\mathrm{d}\sigma_{11} \frac{\partial \widetilde{u}_1}{\partial x_1} + \mathrm{d}\sigma_{22} \frac{\partial \widetilde{u}_2}{\partial x_2} + \mathrm{d}\sigma_{12} \left(\frac{\partial \widetilde{u}_1}{\partial x_2} + \frac{\partial \widetilde{u}_2}{\partial x_1} \right) \right] \mathrm{d}\Omega + \\
& \int_\Omega \left[-\nabla \mathrm{d}\varphi \cdot \nabla \widetilde{\varphi} + \widetilde{\varphi} \frac{e}{\varepsilon_0} \left(\frac{\mathrm{d}n_i}{\mathrm{d}\varphi} \mathrm{d}\varphi - \frac{\mathrm{d}n_e}{\mathrm{d}\varphi} \mathrm{d}\varphi - \mathrm{d}n_d^\star n_{d0} Z_d \right) \right] \mathrm{d}\Omega
\end{aligned} \tag{34}$$

We note that, in deriving (34), we made use of the property $\mathrm{d}\widetilde{\boldsymbol{u}} = \mathbf{0}$ but note that $\mathrm{d}\widetilde{\boldsymbol{u}}^{\bullet} \neq \mathbf{0}$. The Newton solution is based on the two definitions (33-34) using standard techniques (see, e.g. [29]).

4 Petrov-Galerkin discretization

In terms of discretization, we introduce the interpolations for a given element e. Use is made of the interpolation matrices $\boldsymbol{N}_e(\boldsymbol{\xi})$ for $\boldsymbol{u}_d$ and $\mathbf{N}_e(\boldsymbol{\xi})$ for scalars $n^\star$ and φ, with $\boldsymbol{\xi}$ being the parent-domain coordinates. Introducing the nodal unknowns (trial functions) for a given element e ($\boldsymbol{u}_e$, $n^\star$, and φ_e), we have the interpolations:

$$\boldsymbol{u}_d = \boldsymbol{N}_e\left(\boldsymbol{\xi}\right)\boldsymbol{u}_e \tag{35}$$
$$n^\star = \mathbf{N}_e\left(\boldsymbol{\xi}\right)\boldsymbol{n}_e^\star \tag{36}$$
$$\varphi = \mathbf{N}_e\left(\boldsymbol{\xi}\right)\varphi_e \tag{37}$$

For the Galerkin projection (33) we require the test functions:

$$\widetilde{\boldsymbol{u}} = \boldsymbol{N}_e\left(\boldsymbol{\xi}\right)\widetilde{\boldsymbol{u}}_e \tag{38}$$
$$\widetilde{\boldsymbol{u}}^{\bullet} = \boldsymbol{N}_e^{\bullet}\left(\boldsymbol{\xi},\boldsymbol{u}_e\right)\widetilde{\boldsymbol{u}}_e \tag{39}$$
$$\widetilde{n}^\star = \mathbf{N}_e\left(\boldsymbol{\xi}\right)\widetilde{\boldsymbol{n}}_e^\star \tag{40}$$
$$\widetilde{\varphi} = \mathbf{N}_e\left(\boldsymbol{\xi}\right)\widetilde{\varphi}_e \tag{41}$$

where

$$\mathbf{N}_e(\boldsymbol{\xi}) = \left[N_1(\boldsymbol{\xi})\cdots N_{nne}\left(\boldsymbol{\xi}\right)\right] \tag{42}$$
$$\boldsymbol{N}_e\left(\boldsymbol{\xi}\right) = \begin{bmatrix} N_1(\boldsymbol{\xi}) & 0 & N_2(\boldsymbol{\xi}) & \cdots & N_{nne}(\boldsymbol{\xi}) & 0 \\ 0 & N_1(\boldsymbol{\xi}) & 0 & N_2(\boldsymbol{\xi}) & \cdots & N_{nne}(\boldsymbol{\xi}) \end{bmatrix} \tag{43}$$
$$\boldsymbol{N}_e^{\bullet}\left(\boldsymbol{\xi},\boldsymbol{u}_e\right) = \begin{bmatrix} N_1^{\bullet}\left(\boldsymbol{\xi},\boldsymbol{u}_e\right) & 0 & N_2^{\bullet}\left(\boldsymbol{\xi},\boldsymbol{u}_e\right) & \cdots & N_{nne}^{\bullet}\left(\boldsymbol{\xi},\boldsymbol{u}_e\right) & 0 \\ 0 & N_1^{\bullet}\left(\boldsymbol{\xi},\boldsymbol{u}_e\right) & 0 & N_2^{\bullet}\left(\boldsymbol{\xi},\boldsymbol{u}_e\right) & \cdots & N_{nne}^{\bullet}\left(\boldsymbol{\xi},\boldsymbol{u}_e\right) \end{bmatrix} \tag{44}$$

In definitions (42-44), *nne* is the number of nodes in each element, here taken as 4 (low-order quadrilateral) and (cf. [30])

$$N_K^{\bullet}\left(\boldsymbol{\xi},\boldsymbol{u}_d\right) = N_K(\boldsymbol{\xi}) + \frac{\alpha h}{2}\frac{\boldsymbol{u}_{di}}{\|\boldsymbol{u}_d\|}\frac{\partial N_K}{\partial \boldsymbol{x}_i} \tag{45}$$

where α is a stabilization parameter, and h is the *element* characteristic length. The optimal value of α is given by [30]:

$$\alpha = \coth Pe - \frac{1}{Pe} \tag{46}$$

where the Péclet number is defined as

$$Pe = \|\boldsymbol{u}_d\|\, h/2\nu \tag{47}$$

Table 2: Properties used in the numerical examples (provided by [28])

	Value
Z_d	1000
n_{d0}	1×10^{8} m^{-3}
n_{i0}	3×10^{11} m^{-3}
n_{e0}	2×10^{11} m^{-3}
ξ	0 Nsm^{-2}
μ	1.63×10^{-4} Nsm^{-2}
T_e	6.24151×10^{17} K (cf. Eq. 24)
T_i	6.24151×10^{17} K (cf. Eq. 24)
m_d	1.05893×10^{-12} kg$^{\bullet}$
λ_e	121907.0 m
λ_i	99536.8 m
c_{da}	90209.7 ms^{-1}
T^d	12.008 s
$\varphi^{\star}$	5.37844×10^{13} NC^{-1}m
$\bullet$	$m_d = \frac{4\pi\rho_d}{3} r_d^3$
	$r_d = 4 \times 10^{-6}$ and $\rho_d = 3950$ kgm^{-3}(Al_2O_3)

This corresponds to the Streaming Upwind Petrov-Galerkin (SUPG) [24, 30], specializing the element size from the velocity. The *element* characteristic length, h, is defined in agreement with Tezduyar and Park [31], as:

$$h = \frac{2\left\|\boldsymbol{u}_d\right\|}{\sum_{K=1}^{nne}\left|\frac{\partial N_K}{\partial X_i} u_{di}\right|} \tag{48}$$

where N_K are the shape functions and nne denotes the number of nodes in each element. We use the isoparametric interpolation [32]. For a low-order quadrilateral we have $nne = 4$, and the shape functions have the following form:

$$N_K(\boldsymbol{\xi}) = \frac{1}{4}\left(1+\xi_1\xi_{1K}\right)\left(1+\xi_2\xi_{2K}\right) \tag{49}$$

$$\{\xi_{1K}\} = \{-1, 1, 1, -1\} \tag{50}$$

$$\{\xi_{2K}\} = \{-1, -1, 1, 1\} \tag{51}$$

5 Numerical examples

We implemented a specific finite element in SimPlas [33] and used the properties that are shown in Table 2 for the following two examples. The core source code for this element is available. In the first example we assess the nonlinear effects in a short element slab, comparing time-step and mesh dependencies as well as

the effect of viscosity. In the second example, a variable-width slab is presented, which produces a slowly moving vortex.

5.1 Nonlinear effects on a short element slab, $L \cong 5\lambda_i$

We introduce a simple benchmark which consists of a rectangular slab. The left edge of the slab has an imposed electrostatic potential which is constant in time. Two cases are considered, $\overline{\varphi} = -1 \times 10^{10}$ NC^{-1}m and $\overline{\varphi} = -1 \times 10^{12}$ NC^{-1}m. Relevant data is shown in Figure 2 and results for the monitored quantities (u_1, $\varphi/\varphi^\star$ and $n_d^\star$ as functions of time) are presented. To test the robustness with respect to spatial and time discretizations, five meshes are used from 50 up to 220 longitudinal *square* elements. Time steps are 5×10^{-2} s up to 5×10^{-1} s. Figure 2 shows the effect of time-step size and Figure 4 shows the effect of mesh size for this problem. We note some sensitivity to both parameters, but similar to what occurs in nonlinear structural problems. Viscosity has a marked effect, also, and a parametric study is shown in Figure 5.

With the purpose of clearly representing the solitary wave for case B, we deactivate the upper and lower boundary conditions (which were $\boldsymbol{u}_d = \mathbf{0}$) and scaled the $x-$ dimension $5\times$. A depiction of the solitary wave is presented in Figure 6. The presence of a solitary wave can be seen, but no evidence of shock waves was detected.

5.2 Vortex in a variable width slab

In this test, we introduce a change of section in the direction of flow with the goal of testing the robustness of our combination Petrov-Galerkin/Backward Euler integration. Figure 7 shows the dimensions and relevant data for this slab. Time-step sensitivity was found to be very good with the larger time step $\Delta t = 0.5$ s providing acceptable detail. In terms of mesh sensitivity, we test 4 meshes, all with square elements. Only slight dependence is observed, cf. Figure 8. Contour plots for u_1, u_2, n_d, φ and ω are shown in Figure 9. We can observe the smooth behavior of most quantities, with oscillations in n_d, attributed to the change in section.

The 3D version of the slab is shown in Figure 10, where the boundary conditions are equivalent to those in 7, but with the zero velocity around the external boundary, except in the symmetry plane, in which $u_3 = 0$. Figure 10 shows another type of vortex, which was found in the inlet section, with a rotation axis parallel to x. The vortex after the jump is also shown in this Figure and is similar to what was found in the 2D example.

Meshes: $50, 80, 90, 100, 110$ elements
along the longitudinal edge

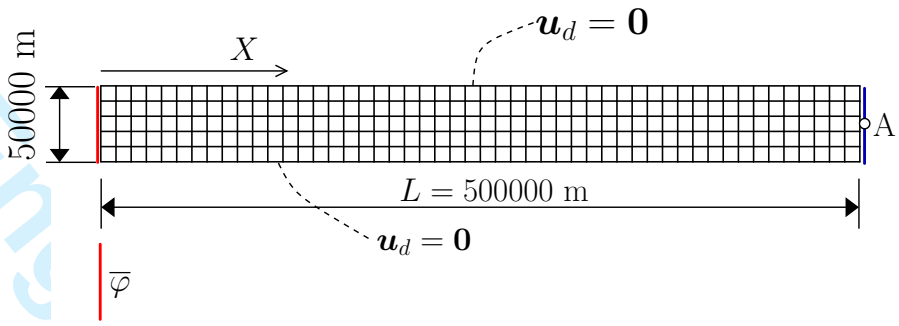

Case A: $\overline{\varphi} = -1 \times 10^{10}$ NC^{-1}m

Case B: $\overline{\varphi} = -1 \times 10^{12}$ NC^{-1}m

$\Delta t \in \{0.05, 0.1, 0.2, 0.5\}$ s

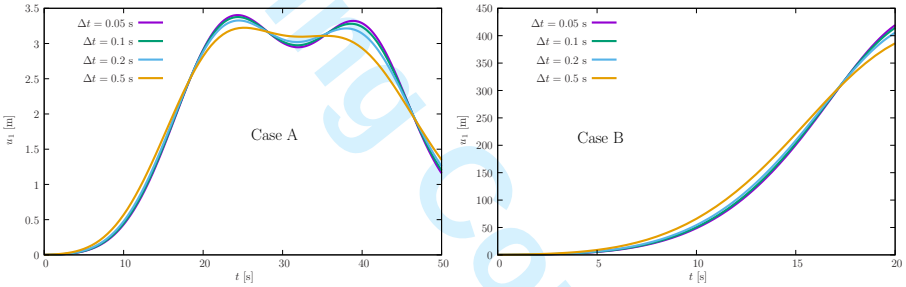

(a) Evolution of u_1 at point A for several values of Δt.

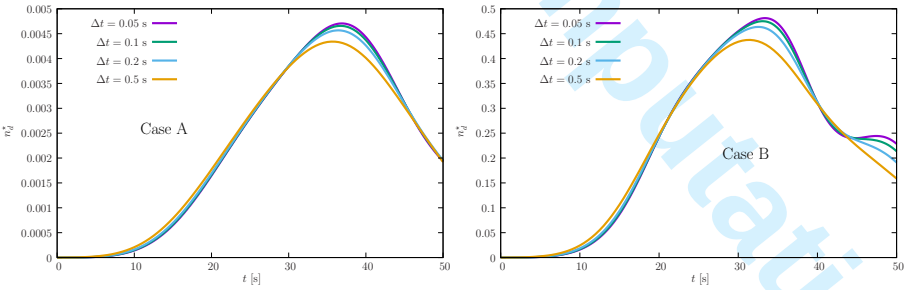

(b) Evolution of $n_d^\star$ at point A for several values of Δt.

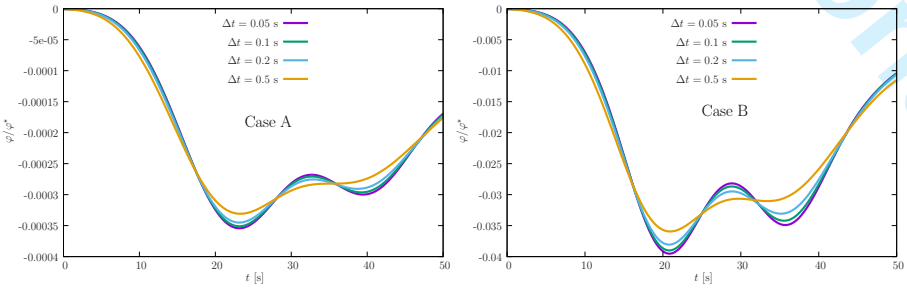

(c) Evolution of $\varphi/\varphi^\star$ at point A for several values of Δt.

Figure 2: Short element slab. Geometry and evolution of u_1, $n_d^\star$ and $\varphi/\varphi^\star$ with time.

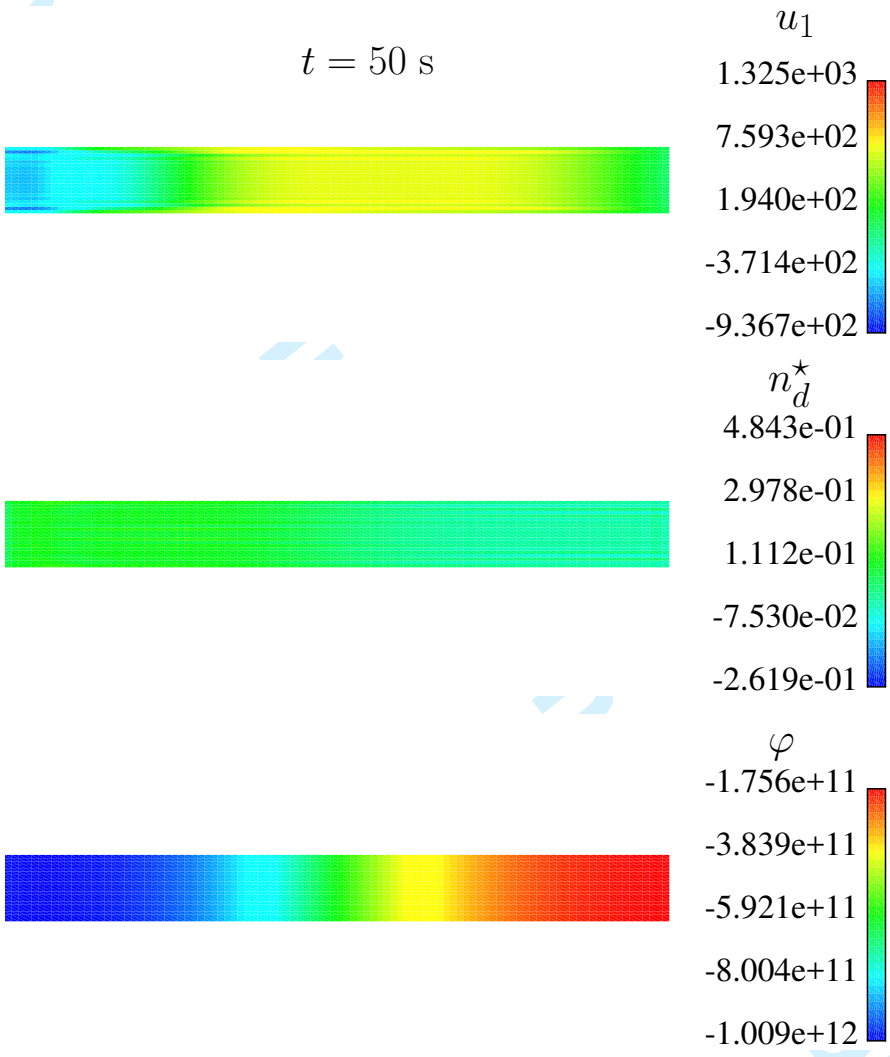

Figure 3: Short element slab. Contour plots of u_1, $n_d^\star$ and φ for $t = 20$ s.

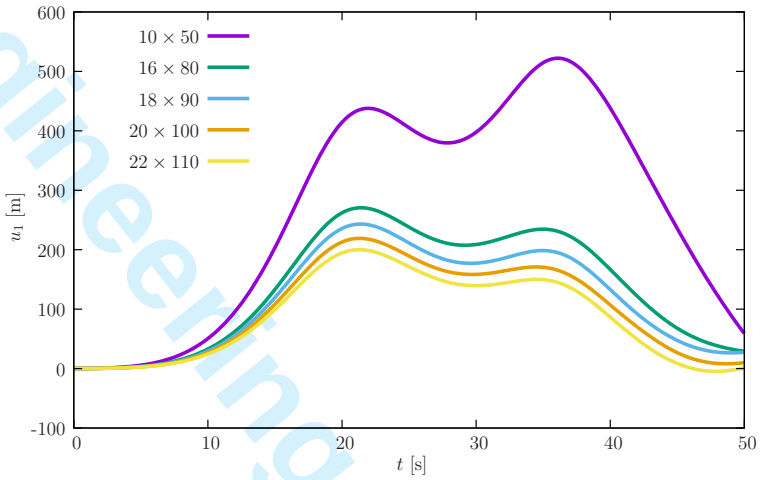

(a) Evolution of u with t for several meshes.

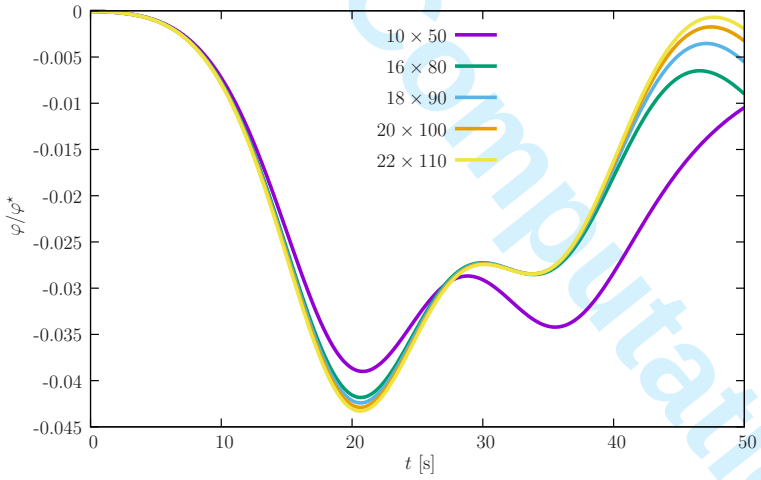

(b) Evolution of $\varphi/\varphi^\star$ with t for several meshes.

Figure 4: Effect of mesh size in the variation of u_1 and $\varphi/\varphi^\star$.

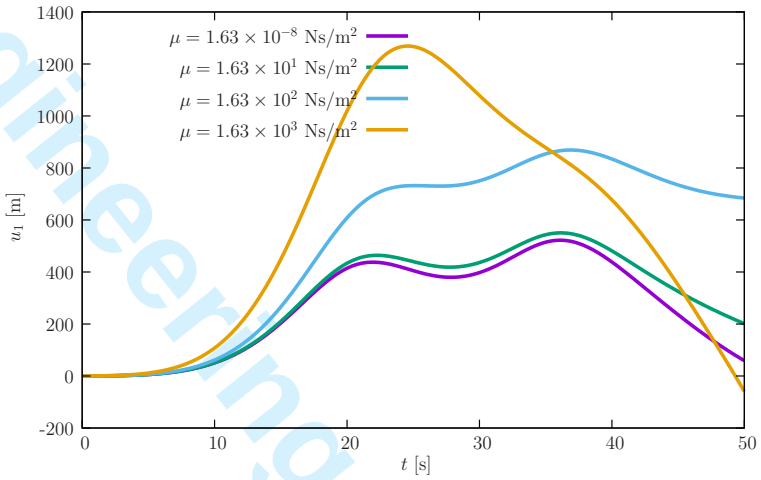

(a) Evolution of u_1 for several values of μ.

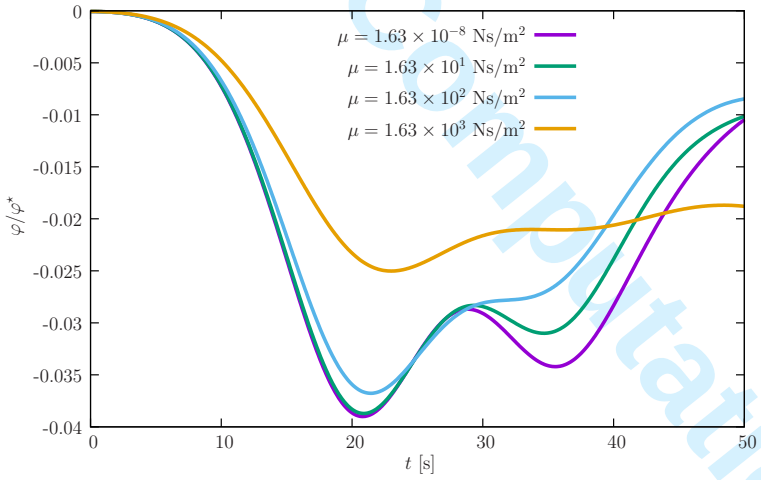

(b) Evolution of $\varphi/\varphi^\star$ for several values of μ.

Figure 5: Effect of μ in the variation of u_1 and $\varphi/\varphi^\star$.

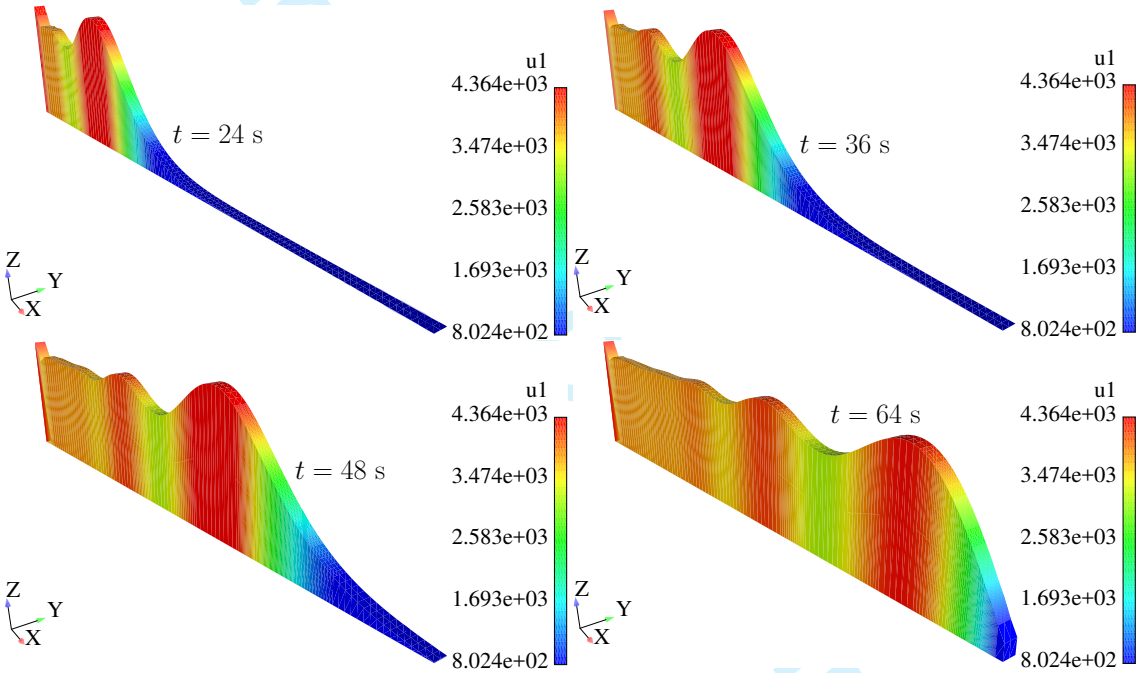

Figure 6: Elongated slab (5×): presence of a solitary wave.

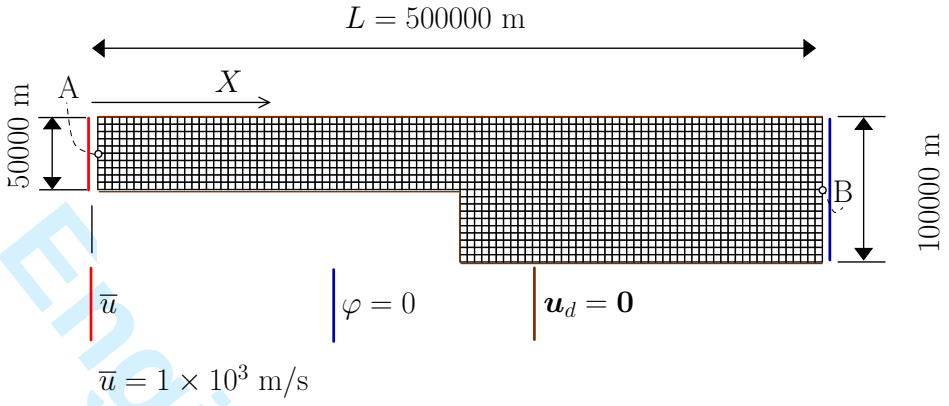

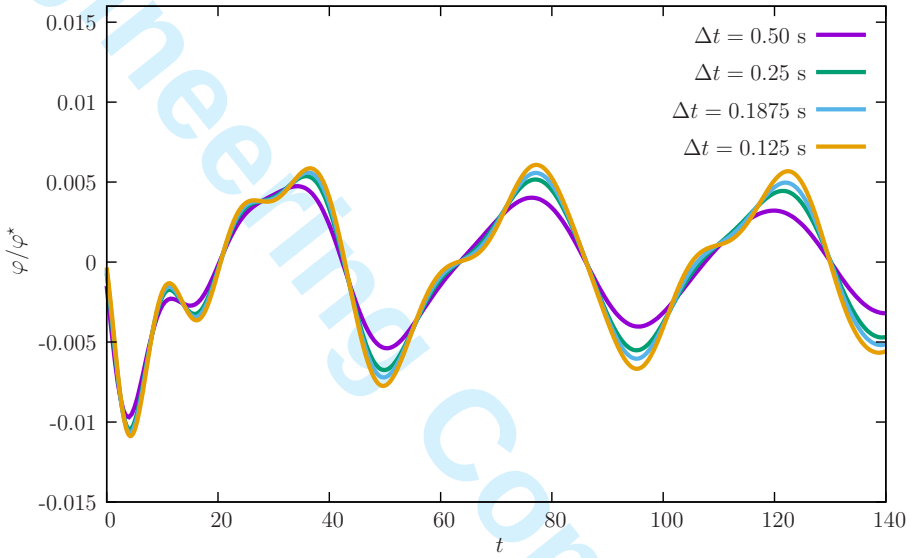

(a) Point **A**: evolution of $\varphi/\varphi^\star$ for four different values of Δt.

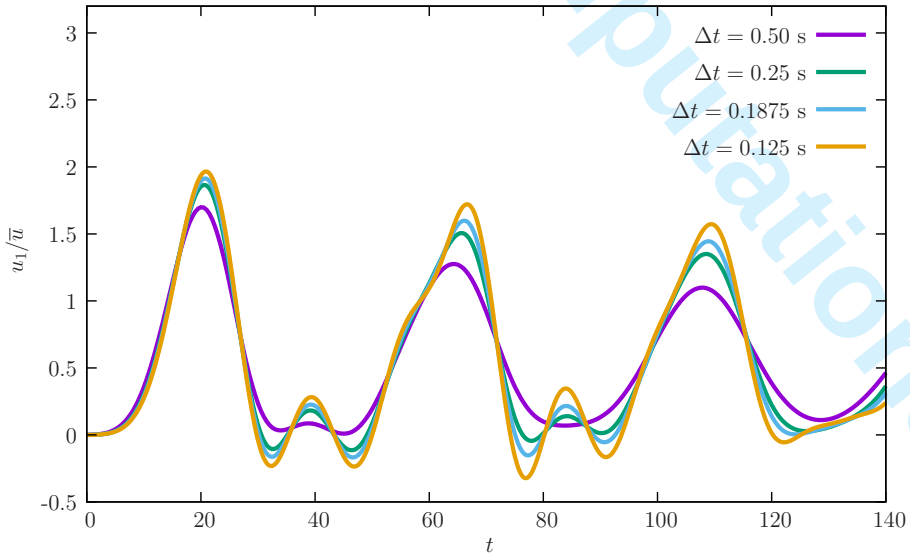

(b) Point **B**: evolution of $u_1/\overline{u}$ for four different values of Δt.

Figure 7: Variable width slab: relevant data and results for u_1 and φ. Points A and B indicate monitored $\varphi/\varphi^\star$ and u_1, respectively.

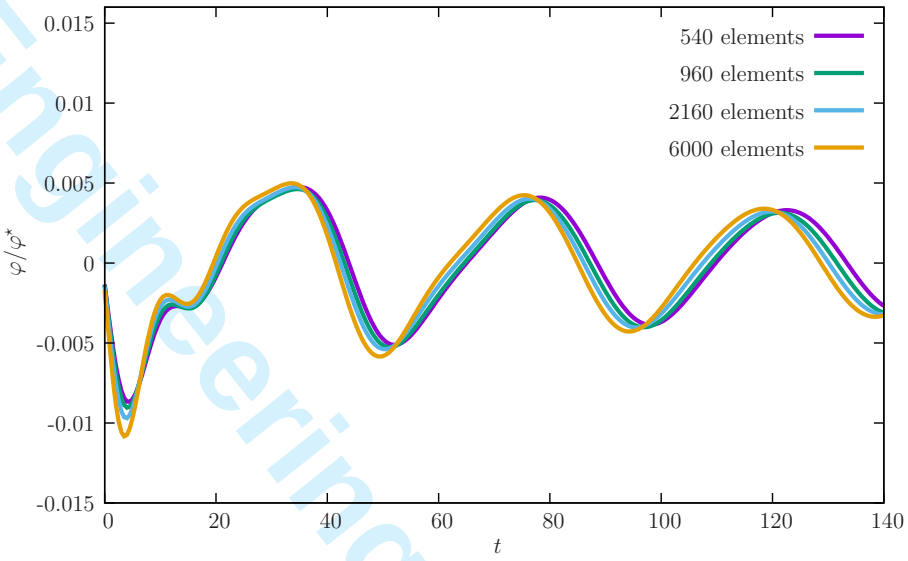

(a) Point **A**: evolution of $\varphi/\varphi^\star$ for four different meshes, $\Delta t = 0.5$ s.

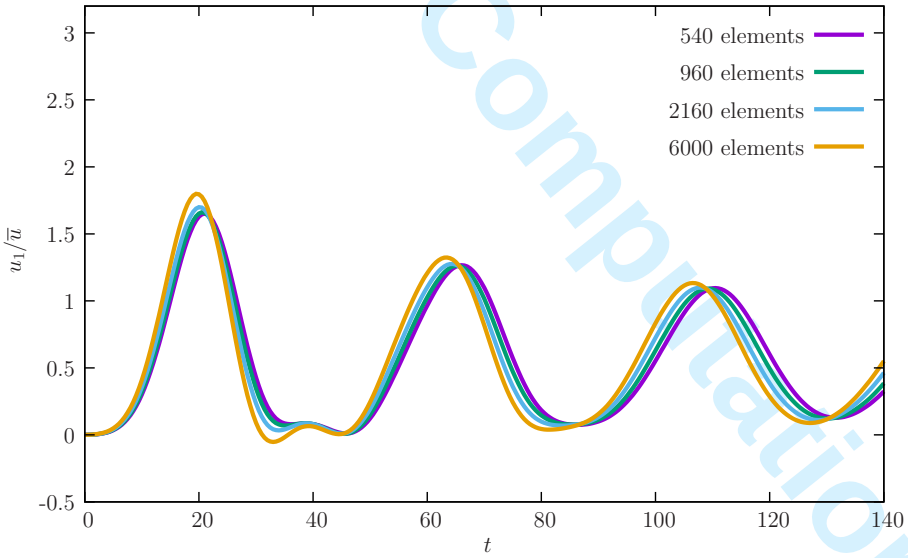

(b) Point **B**: evolution of u_1 for four different meshes, $\Delta t = 0.5$ s.

Figure 8: Variable width slab: relevant data and results for u_1 and φ. Points A and B indicate monitored u_1 and $\varphi/\varphi^\star$, respectively.

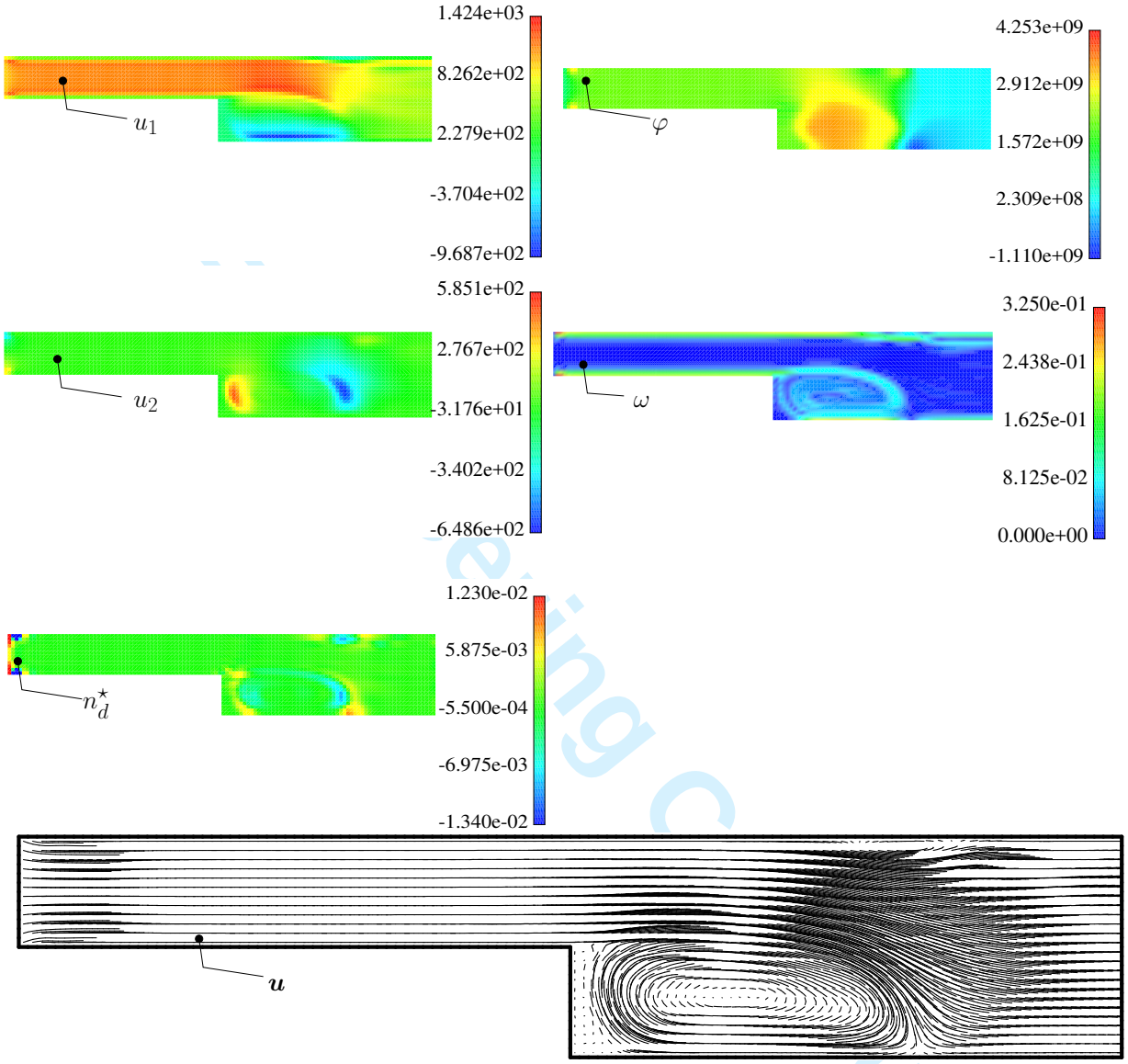

Figure 9: Variable width slab ($t = 500$ s): contour plots for u_1, u_2, φ, $n_d^\star$ and ω. The velocity vectors are also shown.

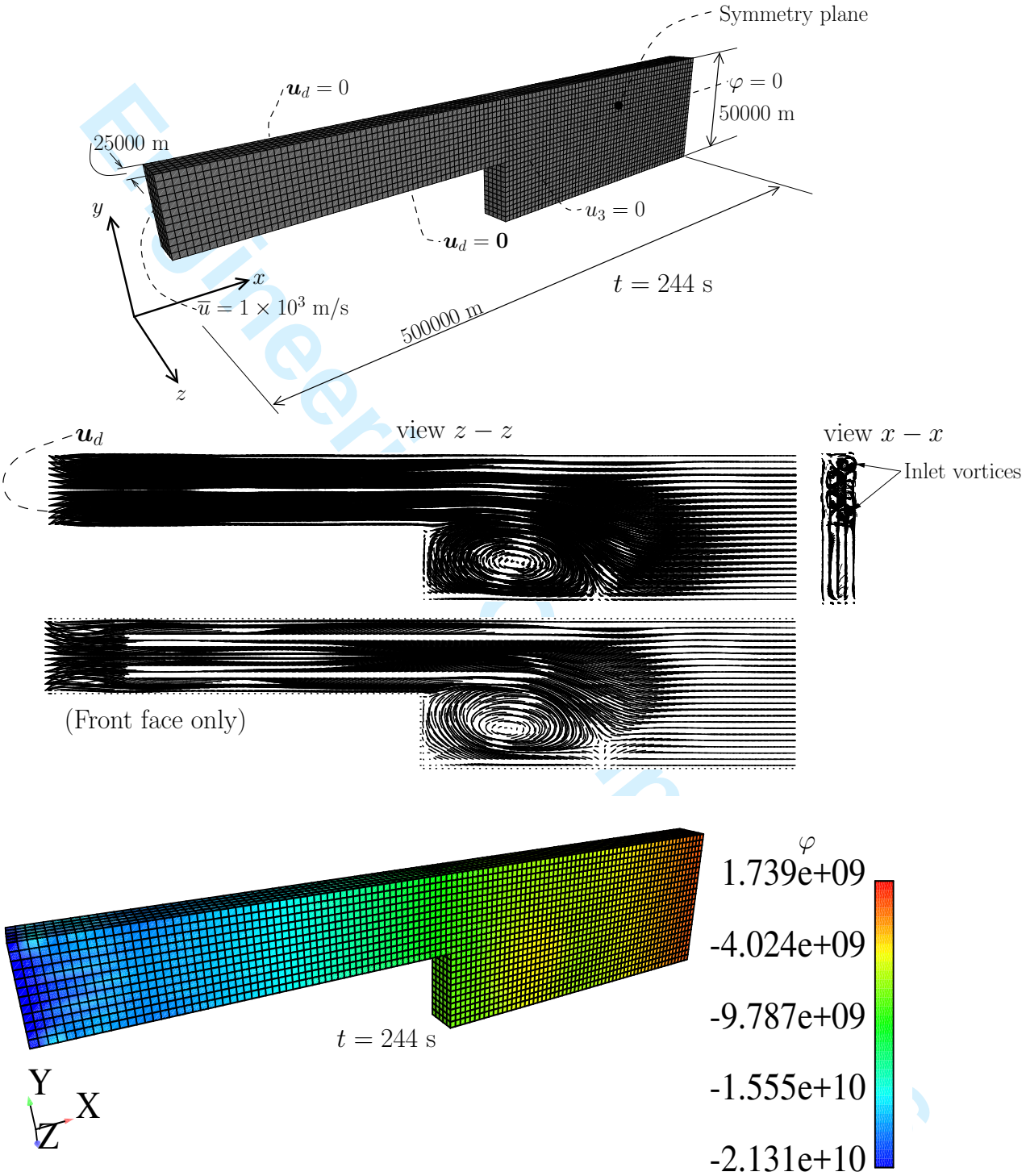

Figure 10: 3D version of the variable width slab. With the addition of a symmetry plane, boundary conditions are similar to those of Figure 8, but additional vortices occur at the inlet.

6 Conclusions

We introduced a new formulation for dust-acoustic waves in unmagnetized plasma including viscosity. This consists of a Petrov-Galerkin finite element combined with the backward-Euler time integration method. Nonlinear effects are included in the number density of ions and electrons, which are affected exponentially by the electrostatic potential. Numerical experiments showed good robustness with respect to mesh size and time-step size and absence of instabilities. Waves resulting from the nonlinear constitutive laws for number densities are sharply observed. In a variable width slab we observe the formation and evolution of a vortex. As a follow-up contribution we will introduce the magnetic field, along with a specialized version of the Maxwell's equations.

References

[1] I. Langmuir. Oscillations in ionized gases. *Proceedings of the National Academy of Science*, 14:627–637, August 1928.

[2] F.F. Chen. *Introduction to plasma physics and controlled fusion*, volume 1: Plasma Physics. Plenum Press, New York, 2 edition, 1984.

[3] P.K. Shukla and A.A. Mamun. *Introduction to dusty plasma physics*. Series in Plasma Physics. IOP Institute of Physics Publishing, 2002.

[4] C.K. Goertz and G. Morfill. A model for the formation of spokes in Saturn's ring. *Icarus*, 53:219–229, 1983.

[5] M. Horanyi, H.L.F. Houpis, and D.A. Mendis. Charged dust in the earth's magnetosphere. *Astrophysics and Space Science*, 144(1-2):215–229, 1988.

[6] R. Merlino and J. Goree. Dusty plasmas in the laboratory, industry, and space. *Physics Today*, 57(7):32–38, 2004.

[7] G.S. Selwyn, J. Singh, and R.S. Bennett. *In situ* laser diagnostic studies of plasma-generated particulate contamination. *J Vac Sci Technol A*, 7(4):2758–2765, 1989.

[8] O. Havnes, C.K. Goertz, G.E. Morfill, E. Grün, and W. Ip. Dust charges, cloud potential, and instabilities in a dust cloud embedded in a plasma. *Journal of Geophysical Research*, 92(A3):2281–2287, 1987.

[9] N.N. Rao, P.K. Shukla, and M.Y. Yu. Dust-acoustic waves in dusty plasmas. *Planet Space Sci*, 38(4):543–546, 1990.

[10] A. Barkan, N. D'Angelo, and R.L. Merlino. Charging of dust grains in a plasma. *Physical Review Letters*, 73(23):3093–3096, 1994.

[11] F.G. Verheest. General dispersion relations for linear waves in multicomponent plasmas. *Physica*, 34:17–35, 1967.

[12] A. Barkan, N. D'Angelo, R.L. Merlino, and C. Thompson. Experiments on ion and dust acoustic waves. In M. Horányi et al., editor, *CP446, Physics of Dusty Plasmas: Seventh Workshop*, pages 97–100. The American Institute of Physics, 1998.

[13] P.K. Shukla and B. Eliasson. Colloquium: Fundamentals of dust-plasma interactions. *Reviews of Modern Physics*, 81:25–44, 2009.

[14] A.A. Mamun and P.K. Shukla. Electrostatic solitary and shock structures in dusty plasmas. *Physica Scripta*, 98:107–114, 2002.

[15] A. Barkan, R.L. Merlino, and N. D'Angelo. Laboratory observation of dust-acoustic wave mode. *Phys Plasmas*, 2(10):3563–3565, 1995.

[16] P.K. Shukla and V.P. Silin. Dust ion-acoustic wave. *Physica Scripta*, 45(5):508, 1992.

[17] C. Sovinec, A. Glasser, T. Gianakon, D. Barnes, R. Nebel, S. Kruger, D. Schnack, S. Plimpton, A. Tarditi, and M. Chu. Nonlinear magnetohydrodynamics simulation using high-order finite elements. *J Comput Phys*, 195(1):355–386, 2004.

[18] C.R. Sovinec and J.R. King. Analysis of a mixed semi-implicit/implicit algorithm for low-frequency two-fluid pasma modeling. *J Comput Phys*, 229:5803–5819, 2010.

[19] S.C. Jardin, J. Breslau, and N. Ferraro. A high-order implicit finite element method for integrating the two-fluid magnetohydrodynamic. *J Comput Phys*, 226:2146–2174, 2007.

[20] B. Srinivasan, A. Hakim, and U. Shumlak. Numerical Methods for Two-Fluid Dispersive Fast MHD Phenomena. *Commun Comput Phys*, 10(1):183–215, 2011.

[21] D. Levy, C.-W. Shu, and J. Yan. Local discontinuous galerkin methods for nonlinear dispersive equations. *J Comput Phys*, 196:751–772, 2004.

[22] S. Garai, S. Jana, M.S. Janaki, and N. Chakrabarti. Stability characteristics of a non-newtonian strongly coupled dusty plasma in the presence of shear flow. *EPL A Letters Journal Exploring the Frontiers of Physics*, 114(65003), 2016.

[23] A.V. Gavrikov, D.N. Goranskaya, A.S. Ivanov, F. Petrov, R.A. Timirkhanov, N.A. Vorona, and V.E. Fortov. Investigation of non-newtonian behavior of dusty plasma liquid. *Journal of Plasma Physics*, 76(3-4):579–592, 2010.

[24] T.J.R. Hughes and A.N. Brooks. A multi-dimensional upwind scheme with no cross wind diffusion. In T.J.R. Hughes, editor, *Finite Elements for Convection Dominated Flows*, number 34, New York, 1979. ASME, AMD.

[25] A. Hasegawa and P.K. Shukla. Dust vortex modes in a nonuniform dusty plasma. *Physics Letters A*, 332:82–85, 2004.

[26] G.K. Batchelor. *An Introduction to Fluid Dynamics*. Cambridge University Press, Cambridge, UK, first edition, 1967.

[27] C. Truesdell and W. Noll. *The non-linear field theories of mechanics*. Springer, third edition, 2004.

[28] H. Fu and W.A. Scales. Model for charged dust expansion. *Physics of Plasmas*, 20:073704, 2013.

[29] K.-J. Bathe. *Finite Element Procedures*. Prentice-Hall, Englewood Cliffs, 1996.

[30] O.C. Zienkiewicz, R.L. Taylor, and P. Nithiarasu. *The Finite Element Method for Fluid Dynamics*, volume 3. Butterworth-Heinemann, Elsevier, 7 edition, 2014.

[31] T.E. Tezduyar and Y.J. Park. Discontinuity capturing finite element formulations for nonlinear convection-diffusion-reaction problems. *Comp Method Appl M*, 59:307–325, 1986.

[32] T.J.R. Hughes. *The finite element method, Linear static and dynamic finite element analyses*. Prentice-Hall, Englewood Cliffs, N.J., 1987.

[33] P. Areias. Simplas. http://www.simplas-software.com.

Corrections performed to the manuscript "*Stable finite element analysis of viscous dusty plasma*" by Areias, Sikta and dos Santos submitted to *Engineering Computations*

August 30, 2017

1 Introduction

We would like to thank the Journal and its Editor, Professor de Souza Neto, for the fair and precise review of the manuscript. We thank the Reviewers for the time and effort spent with this manuscript. We tried to enrich the work so that it values the Journal.

We performed all indicated corrections and introduced more content in the last example (3D vortices), beyond the requested solition wave demonstration. In addition, we slightly changed the text to increase clarity in the notation and further indicate the provenance of all properties in Table 2, including the proof for the temperature values (T_e and T_i).

2 Performed corrections

2.1 Reviewer #1 (recommended Acceptance)

1. **Reviewer #1:** "*The paper addresses the analysis of dust-acoustic waves in unmagnetized plasma including viscosity with a classical Petrov-Galerkin approach for convection-diffusion equations, usually adopted in the framework of finite element solutions of fluid mechanics problems. It is a "multi-physics" problem, in which the unknown fields are the electrostatic potential, the dust density and velocity. It is a very interesting application of known numerical tools on a completely different field, with the necessary adaptations for this specific problem. The paper is clear, well written and the mathematics is flawless. The numerical examples are well chosen to illustrate the capabilities of the code implemented and the solutions are plausible. Nevertheless, the paper would gain immensely if the results, could be validated or confronted, if possible, against other existent solution(s), at least in one or*

two examples. Therefore, in my opinion the paper could be published in its present form, but the validation suggested would be welcomed."
Our corrections: We completely agree with the Reviewer and tried to enrich the manuscript. Validation would be perfect, but this topic is very coarse in terms of experimental data, which is mostly qualitative. We now have a demonstration of the presence of the solitary wave in section 5.1

2.2 Reviewer #2 (recommended Minor Revision)

1. **Reviewer #2:** "*The authors should be demonstrated the main difference between the dust-acoustic waves and dust ion-acoustic waves in the introduction.*"
   Our corrections: we completely agree with the indication and now inserted a description of the difference. We have the highest respect for the book "Introduction to Dusty Plasma Physics" by Shukla and Mamun and use their words: "According to Shukla and Mamun [2], there are two types of acoustic modes in uniform, unmagnetized, collisionless dusty plasmas with a weak Coulomb coupling between the charged dust grains: dust acoustic (DA) and dust ion-acoustic (DIA) waves. In summary,

   (a) In DA waves [1], there is a predominance of *low-frequency* dust grain dynamics with Boltzmann electron and ion distribution.

   (b) In DIA waves [3], dust grains are stationary, electrons follow the Boltzmann distribution and ion dynamics is predominant.

2. **Reviewer #2:** "*It is well known that waves propagating through a plasma medium can transform into a soliton/solitary wave under conditions when the broadening of the wave due to a dispersion effect is balanced by the wave steepening due to nonlinearity. However, if the viscosity effect is included in the plasma system; the balance between the nonlinearity and dispersion is broken and as a result solitons break down and another nonlinear phenomena appears called shock waves or double layers. So, could the author demonstrate how can solitary waves propagate in the plasma system taking into account dust viscosity?*"
   Our corrections: That is very interesting and we provide an answer. Concerning the solition, we obtain a self-similar wave with asymmetric profile created by the nonlinearity in (Eqs. 17-18). We did not mentioned that in the original submission since it requires a long mesh. Now it is in the manuscript. A Figure depicting this is shown here:

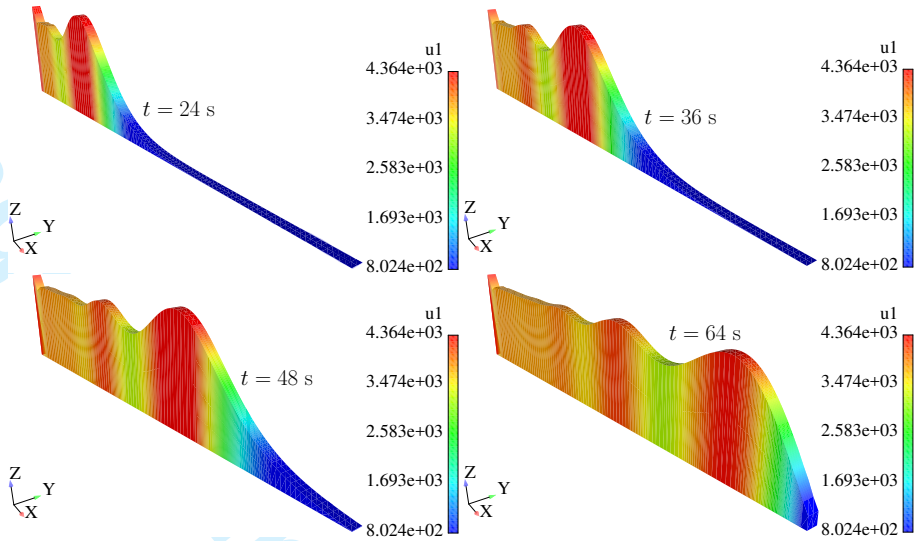

3. **Reviewer #2:** "*This is a very good and novel piece of work. The results of this paper will benefit a lot of researchers in this field. So, I do not have any objection to accept the manuscript after the authors take into account the above comments.*"
   Our corrections: We thank the Reviewer and tried to be clear in what we write.

References

[1] N.N. Rao, P.K. Shukla, and M.Y. Yu. Dust-acoustic waves in dusty plasmas. *Planet Space Sci*, 38(4):543–546, 1990.

[2] P.K. Shukla and A.A. Mamun. *Introduction to dusty plasma physics*. Series in Plasma Physics. IOP Institute of Physics Publishing, 2002.

[3] P.K. Shukla and V.P. Silin. Dust ion-acoustic wave. *Physica Scripta*, 45(5):508, 1992.